Journal of Geophysical Research: Space Physics

RESEARCH ARTICLE
10.1029/2018JA025636

Electron Energy Spectrum and Auroral Power Estimation From Incoherent Scatter Radar Measurements

Ilkka I. Virtanen[1], **Björn Gustavsson**[2], **Anita Aikio**[1], **Antti Kero**[3], **Kazushi Asamura**[4], **and Yasunobu Ogawa**[5]

[1]Ionospheric Physics Research Unit, University of Oulu, Oulu, Finland, [2]UiT – The Arctic University, Tromsø, Norway, [3]Sodankylä Geophysical Observatory, University of Oulu, Sodankylä, Finland, [4]Japan Aerospace Exploration Agency, Japan, [5]National Institute of Polar Research, Tokyo, Japan

Key Points:
- Electron energy spectra are estimated from incoherent scatter radar measurements by integrating the electron continuity equation
- Estimates of upward field-aligned current and auroral power are integrated from the spectrum estimates
- The results are validated using simulations and comparisons with satellite measurements

Correspondence to:
I. I. Virtanen,
ilkka.i.virtanen@oulu.fi

Citation:
Virtanen, I. I., Gustavsson, B., Aikio, A. T., Kero, A., Asamura, K., & Ogawa, Y. (2018). Electron energy spectrum and auroral power estimation from incoherent scatter radar measurements, *Journal of Geophysical Research: Space Physics*, *123*, 6865–6887. https://doi.org/10.1029/2018JA025636

Received 2 MAY 2018
Accepted 23 JUL 2018
Accepted article online 23 JUL 2018
Published online 22 AUG 2018

Abstract Differential energy flux of electrons precipitating into the high-latitude ionosphere can be estimated from incoherent scatter radar observations of the ionospheric electron density profile. We present a method called ELSPEC for electron spectrum estimation from incoherent scatter radar measurements, which is based on integration of the electron continuity equation and spectrum model selection by means of the Akaike information criterion. This approach allows us to use data with almost arbitrary time resolutions, enables spectrum estimation with dense energy grids, avoids noise amplifications in numerical derivatives, and yields statistical error estimates for all the output parameters, including the number and energy fluxes and upward field-aligned currents carried by the precipitating electrons. The technique is targeted for auroral energies, 1–100 keV, which ionize the atmosphere mainly between 80 and 150 km altitudes. We validate the technique by means of a simulation study, which shows that Maxwellian, kappa, and mono-energetic spectra, as well as combinations of those, can be reproduced. Comparison study for two conjugate satellite measurements to the EISCAT UHF radar are shown, for Reimei and Swarm, showing an agreement with the results. Finally, an example of a 2-hr measurement by the EISCAT radar is shown, during which we observe a variety of precipitation characteristics, from soft background precipitation to mono-energetic spectra with peak energies up to 60 keV. The upward field-aligned current varies from 0 to 10 μAm^{-2} and the total energy flux from 0 to 250 mWm^{-2}.

1. Introduction

The energy spectrum of electrons precipitating from the magnetosphere to the ionosphere, the total energy flux, and the upward field-aligned current (FAC) carried by precipitating electrons are key parameters in the studies of magnetosphere-ionosphere (M-I) coupling. The shape of the energy spectrum depends on the source population and the process causing the precipitation. The most commonly observed spectral characteristics within the auroral oval may be categorized into Maxwellian, kappa, mono-energetic (accelerated Maxwellian), and broadband spectra (e.g., McIntosh & Anderson, 2014; Newell et al., 2009). Electrons precipitating from the plasma sheet are best characterized by kappa and Maxwellian distributions (Kletzing et al., 2003). The term *mono-energetic* spectrum comes from the relatively narrow peak in differential energy flux at the peak energy. The interpretation of a mono-energetic spectrum is that it represents acceleration of the (typically Maxwellian) electron population by a quasi-static upward electric field (Evans, 1974; McFadden et al., 1999; Mozer et al., 1980). At energies lower than the peak energy, the differential flux is populated by secondary electrons created in the ionosphere but trapped by the potential drop from above. Sometimes the energy of mono-energetic fluxes rises and falls in the energy-time spectrogram forming an *inverted-V* structure (Frank & Ackerson, 1971), which has been interpreted to stem from a larger-scale U-shaped potential drop (e.g., Karlsson, 2013; McFadden et al., 1999, and references therein). The broadband spectra, where the accelerated electrons have a broad energy range in the parallel direction, but low perpendicular energies, have been suggested to be produced by dispersive Alfvén waves (Chaston, 2003; Keiling, 2009).

While ion-neutral frictional heating is suggested to be the largest M-I power deposition process on the hemispheric scale (e.g., Palmroth et al., 2006, and references therein), the energy flux carried by precipitating electrons (often referred to as auroral power) may dominate on small scales. Diffuse aurora associated with the Maxwellian and kappa distribution fluxes contains majority of the hemispheric precipitation energy flux

(Newell et al., 2009), but much larger energy flux densities are present in auroral arcs and filaments. High fluxes of energetic electrons have been observed in auroral filaments only about 100 m in width (Dahlgren et al., 2012; Lanchester et al., 1997). Since perpendicular electric fields, which cause the ion-neutral frictional heating, may be present both adjacent to auroral arcs (Aikio et al., 2002) and in small-scale structures within an arc (Lanchester et al., 1996), understanding the electrodynamics and the local energy budget associated with aurora requires simultaneous high-resolution observations of electron precipitation and electric fields.

Electron energy spectra can be directly measured by satellite instruments, but the fast moving satellites cannot follow temporal evolution of the highly dynamic structures in the auroral ionosphere. Techniques for estimating electron energy spectra from ground-based incoherent scatter radar measurements thus provide a possibility to follow the temporal evolution of particle precipitation spectra at a given point for extended periods. Various techniques for inverting the electron energy spectrum from the observed electron density profiles have been published since 1970s. UNTANGLE (Vondrak & Baron, 1977) and CARD (Brekke et al., 1989) are steady state models, which assume that the ion production and recombination are in balance. The steady state models are in active use (Miyoshi et al., 2015) and they are also developed further. For example, Simon Wedlund et al. (2013) used the multiplicative algebraic reconstruction technique instead of the maximum entropy method used by Semeter and Kamalabadi (2005), while Kaeppler et al. (2015) used the GLOW electron transport model (Solomon et al., 1988) for calculating electron production rates. The steady state models may be considered more realistic than time-dependent ones when one is interested in the energy spectrum in the frame of reference of an advecting flux tube (Semeter & Kamalabadi, 2005).

By means of time-dependent models, one can relax the stationarity assumption and make reasonable estimates of energy spectra also when electron precipitation varies rapidly, on time scales shorter than the electron recombination time. The SPECTRUM algorithm (Kirkwood, 1988) allows one to make time-dependent fits to EISCAT radar data with predefined spectrum shapes. The inversion technique by Semeter and Kamalabadi (2005) does not use spectrum shape models, but solves the electron number flux in selected energy bins by means of the maximum entropy method. The algorithm by Dahlgren et al. (2011) avoids explicit calculation of electron density time-derivatives by means of iterative fits and numerical integration of the electron continuity equation and implements automatic model selection for finding optimal spectrum shape from among a number of candidate models. The technique used in Turunen et al. (2016) is similar to Dahlgren et al. (2011) in the sense that it models the time-evolution of electron density within each time step, but it relies on a computationally heavy chemistry modeling utilizing the Sodankylä Ion and Neutral Chemistry (SIC) model, because it is targeted for high-energy (>200 keV) electrons and D region ion chemistry. A recent technique by Kaeppler et al. (2015) is a steady state model, but the iterative solution is quite similar with Dahlgren et al. (2011). Time-dependent inversion with a simple spectrum model was used by Vierinen et al. (2016) to demonstrate benefits of incoherent scatter plasma line observations during auroral precipitation.

Another approach to the energy spectrum estimation is taken by Lanchester et al. (1994, 1996, 1997, 1998). The authors use a model including the coupled continuity equations of electrons and several ion and neutral species, electron and ion energy equations, and electron transport. The model uses selected Maxwellian and Gaussian fluxes as input, and the best fitting spectra are estimated by means of finding a sequence of spectra that produce the observed electron densities. Initial values of total energy flux and peak energy are selected by a simple *flux-first* method or using optical data, after which the spectra are tuned until the modeled electron density matches with the observations. This model, together with a combination of radar and optical data, has been used in studies of narrow auroral filaments.

In this paper, we introduce a completely upgraded version of the method used in Dahlgren et al. (2011) to invert electron energy spectra from incoherent scatter radar measurements. We have named the method ELSPEC. The method allows us to estimate electron energy spectra with time resolutions of a few seconds, down to subsecond resolutions in favorable conditions, from which estimates of the upward FAC and the total energy flux are also derived. ELSPEC provides three key benefits. First, it can use data with almost arbitrary time resolution, because it does not calculate derivatives from the discrete data points. The direct calculation of time-derivatives would require that the data are recorded with time steps clearly shorter than the electron recombination time scale at any observed altitude. Second, the technique avoids noise amplification that takes place when two electron density profiles are subtracted in calculation of numerical derivatives. Third, the model selection approach allows us to test with a variety of parametric models of the energy spectrum shape and to automatically select the model that leads to optimal balance between model complexity

and fitting to noise. Furthermore, the method is simple enough to be used as a stand-alone analysis tool and the parametric models allow us to do the calculations with a very dense energy grid. ELSPEC can be run both in time-dependent and steady state modes.

The paper is organized as follows. Section 2 introduces the ELSPEC method in detail. The tool is then tested first with simulated synthetic electron density data in section 3. Results with EISCAT data and comparisons with conjugate Reimei and Swarm satellite observations in two events are shown in section 4. Reliability of the results and necessity of the time-dependent inversion model are discussed in section 5 and conclusions are given in section 6.

2. Inversion of Electron Density Profiles

The ELSPEC technique makes use of the electron continuity equation

$$\frac{\partial n}{\partial t} = Q - \alpha n^2, \tag{1}$$

where n is the electron number density, t is time, Q is the electron (ion) production rate, and α is the effective recombination coefficient. The electron and ion production rates are equal, because the precipitation predominantly produces singly charged positive ions. The electron production rate by impact ionization $Q = Q(I)$ is a known function of the differential electron number flux I [$m^{-2}{\cdot}s^{-1}{\cdot}eV^{-1}$]. The differential energy flux can be calculated from the differential number flux I, which is the unknown in the inversion process.

The key points of the inversion technique are *analytic integration* of the electron continuity equation, fits with *several different models* of the differential number flux, and *model selection* by means of the Akaike information criterion. The spectrum estimation is carried out in the altitude region 80–150 km, where ion production rates of 1–100 keV auroral electrons have their peak values (Fang et al., 2010). At these altitudes, one can usually ignore plasma convection and assume that the main ion species are NO^+ and O_2^+. Convection might sometimes affect the spectrum estimation in presence of strong electric fields associated with auroral arcs. Such events are discussed in sections 4.2 and 5.2.

Since transport of energetic electrons is governed by a set of linear differential equations, we can use the superposition principle and calculate the electron production rate as a sum of production rates at discrete energies E_i. Electron production rates per unit number flux at energies E_i and altitudes h_j are tabulated in matrix **A**, and electron production rates for arbitrary differential number fluxes are calculated as a matrix product

$$\mathbf{Q} = \mathbf{AI}, \tag{2}$$

where **Q** is a column vector of ion production rates at altitudes h_j and **I** is a column vector of differential number fluxes at energies E_i. The ion production rates are calculated with a model by Fang et al. (2010) and the neutral atmosphere, which is needed for the Fang et al. (2010) model, is taken from the NRLMSISE-00 empirical model (Picone et al., 2002). The Fang et al. (2010) model assumes an isotropic pitch-angle distribution in the downgoing hemisphere, which is considered as the most realistic alternative for precipitating electrons at ionospheric altitudes and recommended by Semeter and Kamalabadi (2005) if the distribution is not otherwise known.

The effective recombination coefficients are calculated as

$$\alpha = \alpha_1 p_{NO^+} + \alpha_2 p_{O_2^+}, \tag{3}$$

where p_{NO^+} and $p_{O_2^+}$ are relative abundances of the two ion species and α_1 and α_2 are their dissociative recombination rate coefficients. The coefficients α_1 and α_2 are calculated using the formulas for ground-state ions at temperatures smaller than 1200 K by Sheehan and St-Maurice (2004):

$$\alpha_1 = 3.50 \cdot 10^{-13} \cdot (300/T_e)^{0.69}, \tag{4}$$

$$\alpha_2 = 1.95 \cdot 10^{-13} \cdot (300/T_e)^{0.70}. \tag{5}$$

The electron temperatures are taken from incoherent scatter plasma parameter fits and the ion composition is from the International Reference Ionosphere (IRI) model (Bilitza et al., 2014). The collisional ionization by precipitating electrons causes rapid ion composition variations, which cannot be predicted by IRI. Effects of variable composition are studied quantitatively by means of a chemistry model in section 5.1.

The dissociative recombination rate coefficients for vibrationally excited NO^+ and O_2^+ molecules are significantly smaller than for ground-state ions (Sheehan & St-Maurice, 2004). However, we ignore the vibrationally excited states, because vibrationally excited NO^+ and O_2^+ ions are rapidly converted into ground-state ions in the E region (Pavlov, 2012).

The ELSPEC technique models electron density as function of time, $n_j(t)$, at discrete altitudes, h_j. For each altitude, there is an associated effective recombination rate α_j and an ion production rate Q_j. When the modeled electron densities at altitudes h_j are collected in a vector $\mathbf{n}(t)$, the corresponding effective recombination coefficients in a vector $\boldsymbol{\alpha}$, and the ion production rates are written as matrix product (equation (2)), the electron continuity equations at all altitudes can be collected in the equation

$$\frac{\partial \mathbf{n}}{\partial t} = \mathbf{A}\mathbf{I} - \boldsymbol{\alpha}\mathbf{n}^2, \tag{6}$$

where the multiplications of the vectors in the last term are element-wise.

By means of integrating equation (6), one can solve the electron density as function of time, $\mathbf{n}(t)$. The analytical solution is given by equation (A1). However, the radar measures averaged values of electron densities during the radar integration period. Hence, the modeled discrete electron density values $\mathbf{n}_k$ for the time step k are calculated as

$$\mathbf{n}_k = \frac{1}{\Delta t}\int_{t_{k-1}}^{t_k} \mathbf{n}(t)dt, \tag{7}$$

where Δt is the sample step (radar integration time). The result is given by equation (A2).

The radar data are discrete electron density samples $\mathbf{N}_k$ with error variances $\boldsymbol{\alpha}_k^2$. In the inversion, the residual sum-of-squares

$$SS_L = \sum \frac{\left(\mathbf{N}_k - \mathbf{n}_k\right)^2}{\boldsymbol{\alpha}_k^2} \tag{8}$$

is minimized iteratively.

The inversion makes use of a collection of parametric models of the differential number flux. This collection of models should be able to produce all of the spectrum shapes one can reasonably expect to be observed with the radar. Because the radar beam width is about a kilometer in the E region, and small-scale auroral structures may be only tens of meters wide, the radar observation may be an average from field-lines with different precipitation characteristics. The collection of spectral shapes should thus not be limited to those observed with, for example, high sampling rate satellites above or within the ionosphere, but must be able to produce also more exotic shapes to account for the spatial averaging in the data.

The models of the differential number flux in ELSPEC are of the form

$$\mathbf{I}(\mathbf{P}_L) = \mathbf{E}\exp\left(\sum_{l=0}^{L} P_L(l)\mathbf{E}^l\right), \quad L \geq 1, \tag{9}$$

where $\mathbf{I}(\mathbf{P}_L)$ is a model of the differential number flux [$m^{-2}{\cdot}s^{-1}{\cdot}eV^{-1}$], $\mathbf{P}_L$ is a vector of $L + 1$ polynomial coefficients, and $P_L(l)$ is its lth element. $\mathbf{E}$ is a vector of energy grid points [eV]. The simplest model ($L = 1$) can produce Maxwellians, as well as slightly distorted ones with modest high or low-energy tails. More complex models with higher degree polynomials can produce, for example, very good matches with kappa distributions. We note that one can rather freely choose the parametric models, for example, explicit kappa and Gaussian distributions could be included, but we have not found this necessary.

In practice, criterion (equation (8) is first used to select the best coefficients $\mathbf{P}_L$ for the first order ($L = 1$), the second order ($L = 2$), etc. polynomials. After that, the *corrected Akaike information criterion* (e.g., Burnham & Anderson, 2002) is used to select the optimal model,

$$AIC_L = SS_L + \frac{2(L+1)(L+2)}{M-L}, \tag{10}$$

where M is the number of electron density data points in $\mathbf{N}_k$ and L is the degree of the polynomial. The information criterion values have a minimum at some $L = L_0$. The final fit result for time step k is the differential number flux

$$\mathbf{I}_k = \mathbf{I}(\mathbf{P}_{L_0}) = \mathbf{E} \exp\left(\sum_{l=0}^{L_0} P_{L_0}(l)\mathbf{E}^l\right), \tag{11}$$

where $\mathbf{I}_k$ is a vector of differential number fluxes [$m^{-2}{\cdot}s^{-1}{\cdot}eV^{-1}$] at the energy grid points $\mathbf{E}$.

Derived quantities such as differential energy flux, upward FAC, and total energy flux carried by the precipitating electrons are calculated from the differential number flux $\mathbf{I}_k$. The differential energy flux is obtained from the differential number flux by means of multiplying with the energies E_i, and the total number (energy) flux is obtained by means of integrating the differential number (energy) flux over the whole energy range. The upward FAC carried by these electrons is obtained by means of multiplying the total number flux with the elementary charge.

Goodness of fit is monitored by means of calculating the chi-square estimate

$$\chi^2 = \frac{SS_{L_0}}{M}, \tag{12}$$

where the number of degrees of freedom is approximated as the number of electron density data points M. The number of unknown coefficients, $L_0 + 1$, is not subtracted from M, because a regularizing imaginary measurement is added for each polynomial coefficient, and the number of measurements in the inverse problem is thus effectively $M + L_0 + 1$.

In this form, the inversion works technically well and produces modeled electron densities, which match well with the observations. However, a periodically changing and an essentially constant number flux may produce almost identical discrete electron densities $\mathbf{n}_k$ in certain conditions. The estimated differential number fluxes tend to oscillate in time especially when the electron density in the upper E region is low and electron recombination times are correspondingly long. In order to suppress the unrealistic oscillations, we have implemented a slight modification to the inversion technique. The adaptive integration, explained in Appendix B, uses effectively coarser time resolution in areas with long recombination times, guiding the analysis toward a smooth solution.

Error estimation in ELSPEC is somewhat more complicated than in many other spectrum inversion techniques, because we must take into account the uncertainty in the modeled density $\mathbf{n}(t_{k-1})$, which is absorbed in the numerical time-derivatives in most other inversion techniques. In order to include this inaccuracy, we form an extended vector of unknowns,

$$\mathbf{x} = \left(\mathbf{n}(t_{k-1}); \mathbf{P}_{L_0}\right), \tag{13}$$

where $\mathbf{n}(t_{k-1})$ is the electron density profile at end of time step $k - 1$, and calculate its covariance matrix by means of finite differences from linearized theory in vicinity of the iteration convergence point. This covariance is then used for estimating the covariance matrix of $\mathbf{n}(t_k)$ by means of linear approximations, and covariance matrix of the coefficients $\mathbf{P}_{L_0}$ is extracted from the covariance of $\mathbf{x}$. The covariance matrix of $\mathbf{P}_{L_0}$ is used for estimating the covariance matrix of $\mathbf{I}_k$, from which error estimates of the derived quantities are calculated. This approach allows us to pass the error covariance matrix of the fitted electron densities $\mathbf{n}(t_k)$ between subsequent time steps in the error estimation.

Table 1
Initial Differential Number Fluxes Used in the Simulation

Period	Differential number flux
A	$I_M(E_0 = 1\text{keV}, Q_0 = 2\text{mWm}^{-2})$[a]
B	$I_M(E_0 = 12\text{keV}, Q_0 = 20\text{mWm}^{-2})$
C	$I_\kappa(E_0 = 2\text{keV}, Q_0 = 20\text{mWm}^{-2}, \kappa = 4)$
D	$I_M(E_0 = 1\text{keV}, Q_0 = 2\text{mWm}^{-2}) + I_M(E_0 = 12\text{keV}, Q_0 = 20\text{mWm}^{-2})$
E	$I_M(E_0 = 1\text{keV}, Q_0 = 2\text{mWm}^{-2}) + I_\kappa(E_0 = 2\text{keV}, Q_0 = 20\text{mWm}^{-2}, \kappa = 4)$
F	$I_M(E_0 = 1\text{keV}, Q_0 = 2\text{mWm}^{-2}) + I_n(Q_0, E_0, W = 2keV)$[b]
G	$I_\kappa(E_0 = 2\text{keV}, Q_0 = 2\text{mWm}^{-2}, \kappa = 4) + I_n(Q_0, E_0, W = 2keV)$[b]
H	$I_n(Q_0, E_0, W = 2keV)$[b]

Note. The functions I_M, I_κ and I_n are defined in equations (14), (15), and (16). [a]During the last minute, E_0 increases to 12 keV and Q_0 to 20 mWm^{-2}. [b]E_0 varies from 0 to 30 keV and Q_0 from 0 to 60 mWm^{-2}.

The error estimates are calculated under the assumption that the selected spectrum model can perfectly reproduce the true spectrum. Since the spectrum model is selected based on the observational data, this is an invalid assumption for electron energies that cause ionization mainly below 80 km or above 150 km, corresponding to energies greater than 100 keV and lower than 1 keV, respectively. In practice, the spectrum models in ELSPEC lead to very small error estimates in these regions. Due to error correlations, underestimation of errors turns on gradually, and the errors might be underestimated also within the 1–100 keV energy range, especially at the low-energy end where the altitude profiles of ion production are very smooth.

3. Verification With Simulated Data

Since the number of electron density data points is typically much smaller than the number of energy grid points and the matrix **A** contains significant off-diagonal elements (Semeter & Kamalabadi, 2005), the solution to the spectrum estimation problem is not necessarily unique. In this section the ELSPEC technique is tested by means of analyzing simulated radar data, which correspond to known, time-varying precipitation spectra.

For each time step k of the simulation, a differential number flux with a known functional form is selected. The simulation uses combinations of Maxwellian fluxes,

$$I_M(Q_0, E_0, E) = \frac{Q_0 E}{2E_0^3} \exp\left(-\frac{E}{E_0}\right), \tag{14}$$

kappa distribution fluxes

$$I_\kappa(Q_0, E_0, E, \kappa) = \frac{Q_0 E}{2E_0^3} \frac{(\kappa - 1)(\kappa - 2)}{\kappa^2} \left(1 + \frac{E}{\kappa E_0}\right)^{-\kappa - 1}, \tag{15}$$

and narrow mono-energetic fluxes

$$I_n(Q_0, E_0, E, W) = C_0 E \exp\left(-\frac{(E - E_0)^2}{W^2}\right), \tag{16}$$

where Q_0 is the total energy flux, E_0 is the characteristic energy, C_0 is a scaling factor, and W is a parameter that controls the width of the mono-energetic distribution. All fluxes are isotropic in the downgoing hemisphere. The simulation consists of eight 5-min periods denoted with letters A, B, … , H. The original spectra used in each period of the simulation are listed in Table 1. Our aim is not to simulate only typical conditions, but to include also rather exotic spectra to push the inversion technique to its limits.

The input fluxes for the simulation, $\mathbf{I}_k^s$, are produced by means of adding random noise to spectra calculated with equations (14), (15), and (16). The fluxes $\mathbf{I}_k^s$ are then used as inputs to the electron production and recombination models introduced in section 2 which produce simulated (continuous in time) electron density profiles, $\mathbf{n}^s(t)$, and simulated (discrete) electron density measurements, $\mathbf{N}_k^s$. Random noise is added to the simulated electron densities $\mathbf{n}^s(t_k)$ at each time step. In addition, random noise is added to the simulated

measurements, $\mathbf{N}_k^s$. The simulation is run with 1 s time steps and with 2,000 energy grid points. The simulated measurements are post integrated to 5 s resolution and are analyzed with ELSPEC, using a coarser energy grid (300 points) than in the simulation. The results are shown in Figures 1 and 2.

Figure 1 shows the simulated electron density measurements $\mathbf{N}_k^s$ (first panel), the differential energy fluxes used in the simulation (third panel), the electron density modeled in the inversion (second panel), the estimated differential energy flux (fourth panel), the upward FAC (fifth panel), the total energy flux (sixth panel), and the χ^2 of the fit (seventh panel). In the fifth and sixth panels, the blue curves are the simulation inputs and the black curves with the red error bars are the inversion results.

Comparison of the first and second panels of Figure 1 shows that the electron densities modeled in the inversion match well with the input data. The only clear difference is at 80–90 km altitudes in period G, immediately after the mono-energetic flux has reached its maximum. Although the deviation is clearly visible, one should note that electron density at this altitude is less than 10% of the peak density around 100 km altitude, and the error is only a few percent of the maximum. Difference of the input and modeled densities (not shown) reveals that differences larger than the statistical error of the input density are seen close to the lower boundary of the ionization in periods F, G, and H. These are associated with the larger χ^2 values in the bottom panel. Peaks in χ^2 around 00:05 and 00:10, at sharp gradients in energy fluxes, are caused by deviations over a larger altitude interval and cannot be easily recognized in visual inspection.

The inverted energy spectra in the fourth panel match very well with the known simulation input in the third panel during periods A, B, and C. These are the periods with Maxwellian and kappa distribution fluxes. Main characteristics of the dual-peak distribution in period D are also clearly visible, although the low-energy peak is missing from some time steps. Also, the sum of a Maxwellian and a kappa distribution in period E is reproduced well in general, though some oscillations in time are seen in the lowest energies. Peak energies of the mono-energetic fluxes in periods F, G, and H are correct, but the distributions tend to be slightly too wide, which is a possible reason for the observed mismatch in electron densities. The weak background fluxes in periods F and G are essentially invisible to the inversion when the mono-energetic flux is much larger than the background flux. This is to be expected, because the background flux has only a minor effect on the electron density profiles in these cases.

The estimates of FAC in the fifth panel and the total energy flux (power) in the sixth panel match remarkably well with the simulation input. The current estimates tend to be more noisy than the power estimates, because they have more contribution from the low energies, where the inversion typically is less accurate. Deviations from the true current are oscillations around the true value, and systematic bias is not visible in the results. However, deviations from the correct value are larger than the error estimates during the first half of period F, when peak energy and flux of the mono-energetic spectrum change rapidly. ELSPEC assumes that the spectrum does not change during the 5-s time steps, and a plausible explanation for the differences is violation of this assumption. The total energy flux estimates are very accurate and match well with the true values, even when the inverted spectra show deviations from the simulation inputs.

While Figure 1 shows overall characteristics of the differential energy flux, comparison of individual differential number flux estimates is shown in Figure 2. Each panel of the figure show a result from one 5-s time step. The blue curve is the simulation input (including the added noise), the black curve is the inversion result, and the red area covers the 1-σ error estimates. The figure indicates very similar findings as Figure 1. The inversion results from periods A, B, and C make a perfect match with the simulation input. The other periods reveal the main characteristics of the spectra, but the more exotic distributions may not be perfectly reproduced in the inversion. When the distributions have two maxima (D, F, and G), the maximum at higher energy is well reproduced, but the secondary maximum at lower energy is not as well modeled.

As a conclusion, the inversion is well capable of finding the characteristic energies and main characteristics of the spectrum shape. However, as one can reasonably expect, the characteristics with largest fluxes and strongest induced ionization are best visible, while weaker features are more difficult to reproduce. Estimates of the FAC are very accurate, the known input value being within the statistical error estimates almost always. However, the combination of a time-varying mono-energetic flux and a weaker low-energy background did cause some oscillations in the current estimates. Finally, the total energy flux estimates are of excellent quality, even in situations when the spectrum shape is not.

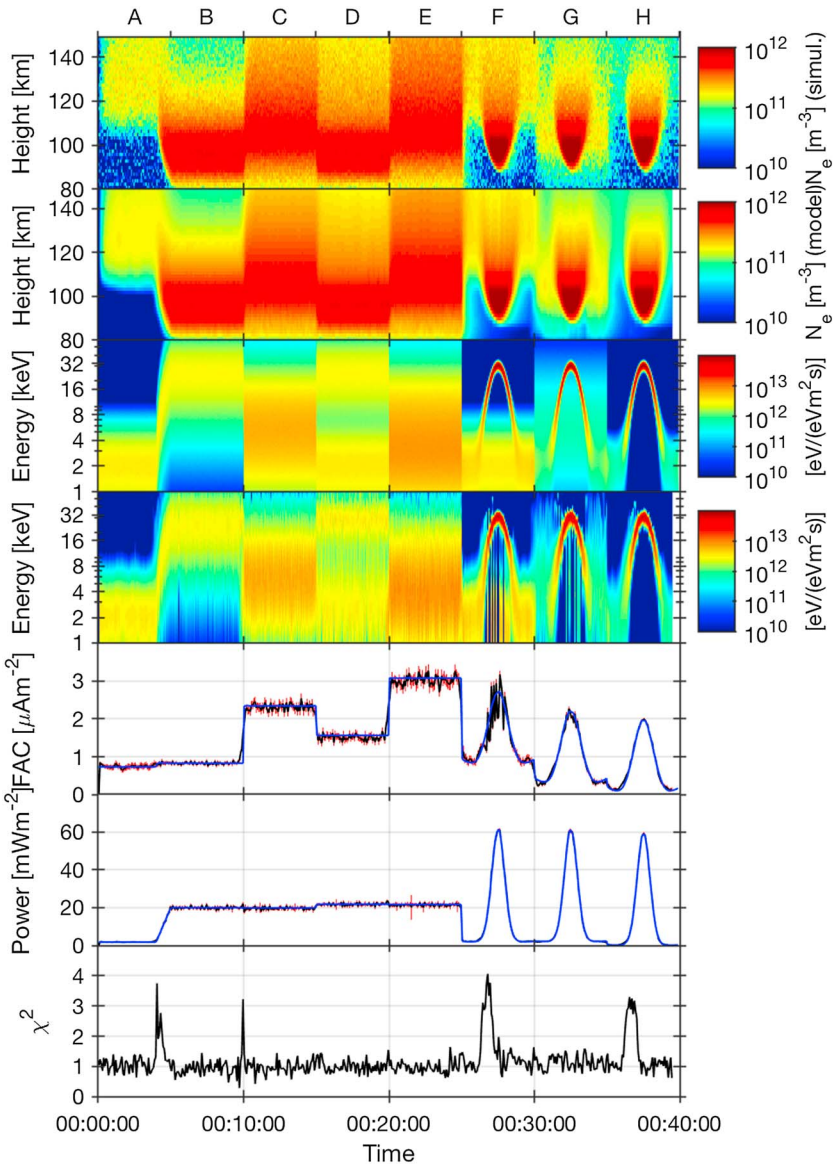

Figure 1. ELSPEC analysis results with simulated data. Simulated electron density (first panel), modeled electron density (second panel), differential energy flux used in the simulation (third panel), inverted differential energy flux (fourth panel), upward FAC (fifth panel), total energy flux (sixth panel), and χ^2 (bottom panel). The blue curves are the known simulation inputs and the black curves with red error bars are the inversion result. Details of the input spectra are given in Table 1.

4. EISCAT Analysis Results

We have searched for events with the criteria that there was a satellite conjunction with the EISCAT UHF radar, where the satellite observed either electron energy spectra or FAC, the UHF radar observed the E region and was pointed field-aligned, the Sun was below the horizon, and electron precipitation occurred during the satellite conjunction. We show two such events in this section.

In both events, the standard GUISDAP analysis software (Lehtinen & Huuskonen, 1996) is used to estimate electron density, electron temperature, ion temperature, and line-of-sight ion velocity from EISCAT data with 1 min resolution. The electron densities are calibrated by means of comparing the E region peak densities to measurements from the colocated Tromsø dynasonde (Rietveld et al., 2008). So-called raw electron densities, essentially weighted backscatter power profiles, are estimated in a second GUISDAP run with 4 or 5 s time resolution. The raw electron density is equal to the true density if electron and ion temperatures are equal,

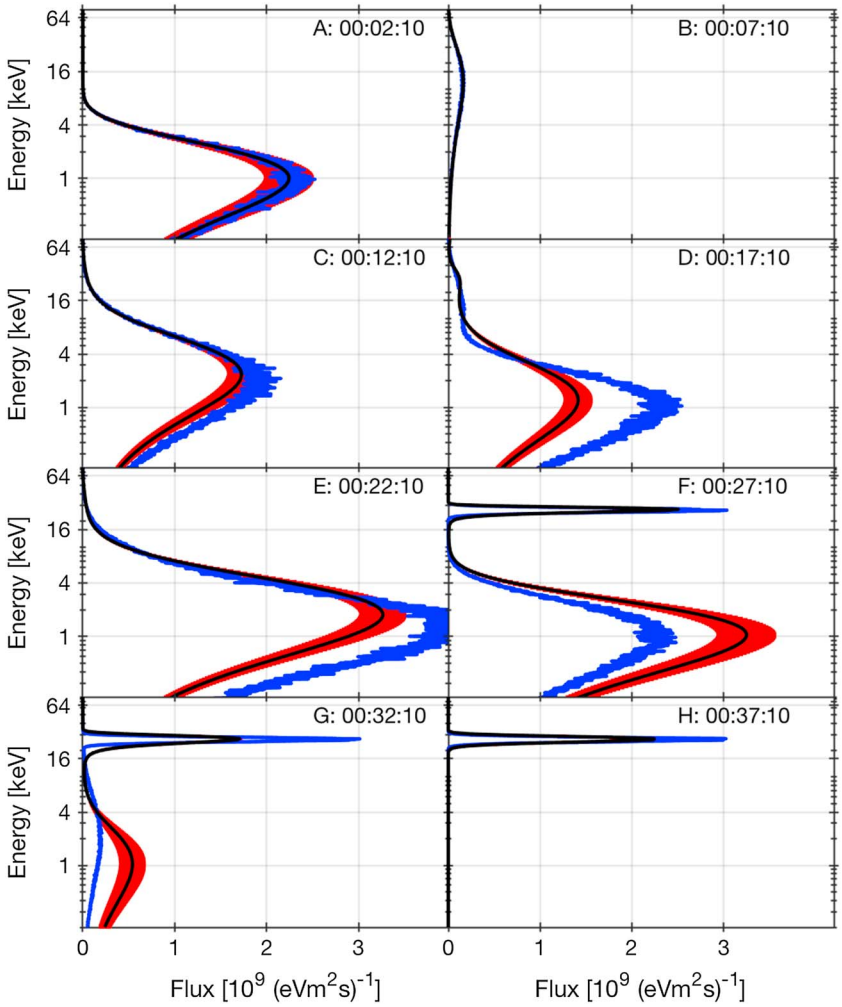

Figure 2. Differential number fluxes from ELSPEC analysis of simulated data. The blue curves are simulation inputs and the black curves with red error bars are the inversion results. The samples are taken with 5-min steps from the simulation results, each corresponding to a different spectrum in the simulation as follows. (a) a Maxwellian, (b) a Maxwellian, (c) a kappa distribution, (d) sum of two Maxwellians, (e) sum of a Maxwellian and a kappa distribution, (f) sum of a Maxwellian and a mono-energetic distribution, (g) sum of kappa and mono-energetic distributions, and (h) a mono-energetic distribution. Details of the input spectra are given in Table 1.

which is typically a good approximation in the E region (Semeter & Kamalabadi, 2005). The electron temperature estimates are interpolated to the higher time resolution of the raw electron density estimates by means of linear interpolation. The electron temperature estimates are needed for calculating the effective recombination coefficients in equations (4) and (5).

4.1. REIMEI Conjunction 5 December 2007

On 5 December 2007, the Reimei satellite (Saito et al., 2005) was moving from north to south and had a close conjunction with the EISCAT Tromsø radars from 00:36:35 to 00:36:45 UT, when the EISCAT UHF radar was running the arc1 modulation in the field-aligned direction. The modulation is an alternating code with 900 m height resolution and 4 s time resolution. The data are available also with 0.44 s resolution, but the 4 s resolution is used in this study in order to improve the statistical accuracy of the measurements. The radar observes ionization from particle precipitation with peak density around 120 km altitude. The raw electron densities and inverted energy spectra are shown in Figure 3. The observed electron density (top panel) is very stable, and the analysis indicates a stable electron flux with a peak energy around 4 keV (third panel). The precipitation produces an upward FAC with a current density around 1.3 μAm^{-2} (fourth panel) and with an energy flux around 5 mWm^{-2} (fifth panel). Both the modeled electron density (second panel) and the χ^2 estimates (bottom panel) indicate a very good match between the observed and modeled densities.

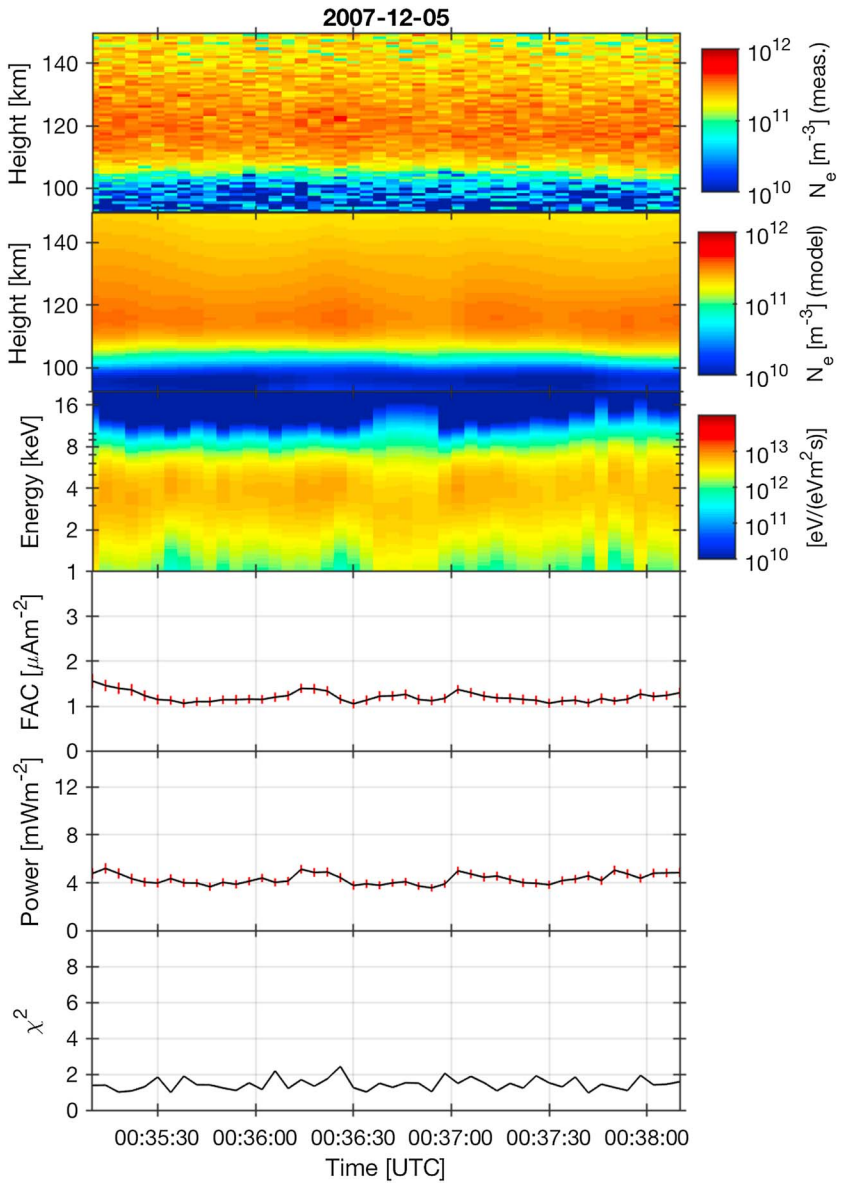

Figure 3. Inversion results during the Reimei satellite overflight on 5 December 2007, 00:36:39 UT. Observed electron density (top panel), modeled electron density (second panel), differential energy flux (third panel), upward FAC (fourth panel), total energy flux (fifth panel), and χ^2 (sixth panel).

Comparison of the inverted differential number fluxes and direct satellite observations with the Reimei Electron Spectrum Analyzer (ESA) instrument (Asamura et al., 2003) are shown in Figure 4. The ESA instrument has several channels covering different pitch-angle ranges. For this comparison, all electrons going downward at the satellite altitude of 634 km are integrated together. Altitude adjusted corrected geomagnetic (aacgm_v2) coordinates (Shepherd, 2014) are calculated for both the EISCAT field-line and the satellite. The ESA instrument was sampled with a time resolution of 40 ms, producing 100 samples during each time step of the ELSPEC analysis. We have selected the two 4-s time intervals, during which the satellite was closest to the geomagnetic latitude of the radar. At this time, the separation in magnetic longitude was about 1.2°, and shortest distance from the satellite to the radar beam was about 65 km. Band-like multiple auroral arcs along the geomagnetic longitude were seen above Tromsø during the close conjunction. The individual dots in Figure 4 are the individual measurements from the ESA instrument. The dotted line is an average of the individual measurements from each energy channel of the ESA instrument. The continuous black line is the ELSPEC inversion

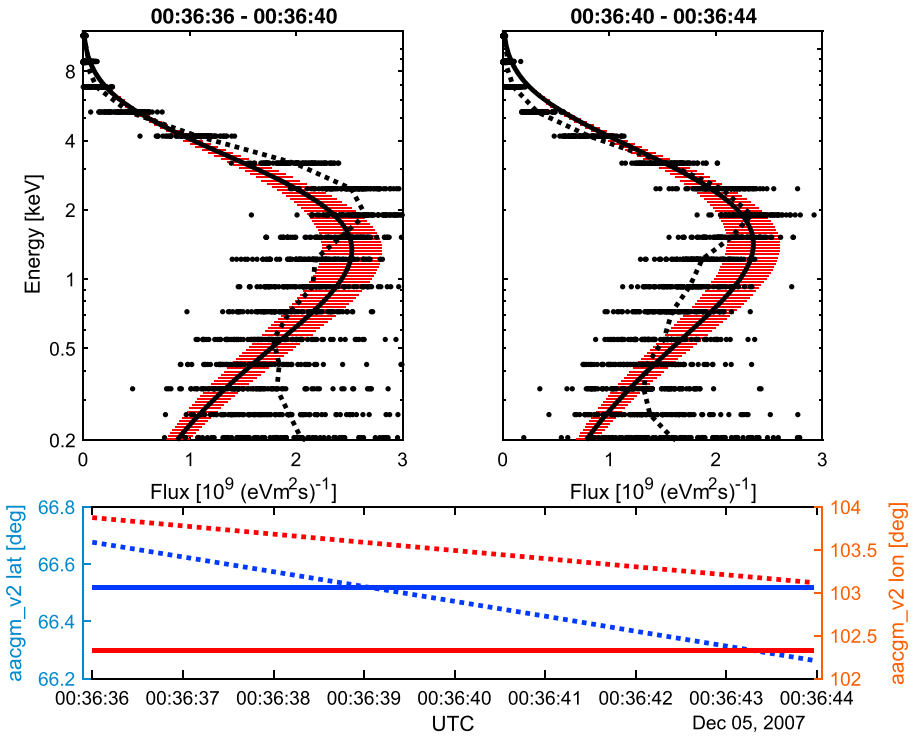

Figure 4. Comparison of differential number fluxes estimated with ELSPEC and in situ observations from the Reimei satellite. Upper panels: differential number fluxes from two 4-s radar integrations. The dots are individual data points from the Reimei Electron Spectrum Analyzer instrument and the dotted line is mean of the Reimei Electron Spectrum Analyzer data points. The continuous line is the ELSPEC inversion result and the red bars are 1-σ error estimates. Bottom panel: aacgm_v2 coordinates of the satellite (dotted lines) and EISCAT (continuous lines). The satellite is at geomagnetic latitude of EISCAT at 00:36:39 UT.

result from EISCAT data and the horizontal red lines are 1-σ error estimates at each energy grid point of the inversion.

The observations from the satellite and the ELSPEC inversion results make an excellent match, the inversion result being within the distribution of the satellite data points in every energy bin above 200 eV. Especially the upper part of the spectra match well, which is to be expected because the highest energies determine the altitude of the bottom of the ionization, which is a clearly distinguishable feature in the radar data. Below 500 eV the inverted flux decreases rapidly, while the satellite observation has a low-energy tail (which continues to larger fluxes at the lowest energies not shown in the figure). We consider the inversion results below 1 keV unreliable in general, because the low-energy electrons cause ionization mainly above the upper boundary of the inversion at 150 km altitude. As was mentioned in section 2, the spectrum shape is thus determined by electrons above 1 keV alone, although the polynomial coefficients can be used for calculating the spectra down to zero energy. For this reason, also the statistical error estimates at low energies are unrealistically small, as one can see from Figure 4.

4.2. Swarm C Conjunction 9 November 2015

On 9 November 2015, the Swarm C satellite (Olsen et al., 2013) was moving from south to north and passed an auroral arc above Tromsø from 21:38:35 to 21:38:41 UT. The arc was observed also with the EISCAT UHF radar running the beata modulation in the field-aligned direction. The modulation is an alternating code with 3 km height resolution and 5 s time resolution. The observed electron densities and the energy spectrum inversion results are shown in Figure 5. During the first minute shown in the plot, weak ionization is seen above 110 km altitude. After 21:37:30 UT, the density increases first in the upper altitudes. The lower edge of the increased ionization moves downwards, until it reaches 110 km altitude 1 min later, at 21:38:30, after which the density decreases at all altitudes. A local decrease in electron density between altitudes from 115 through 130 km is seen after 21:39:30. After 21:40 UT, the electron density profile is very similar with the profile observed before 21:37 UT.

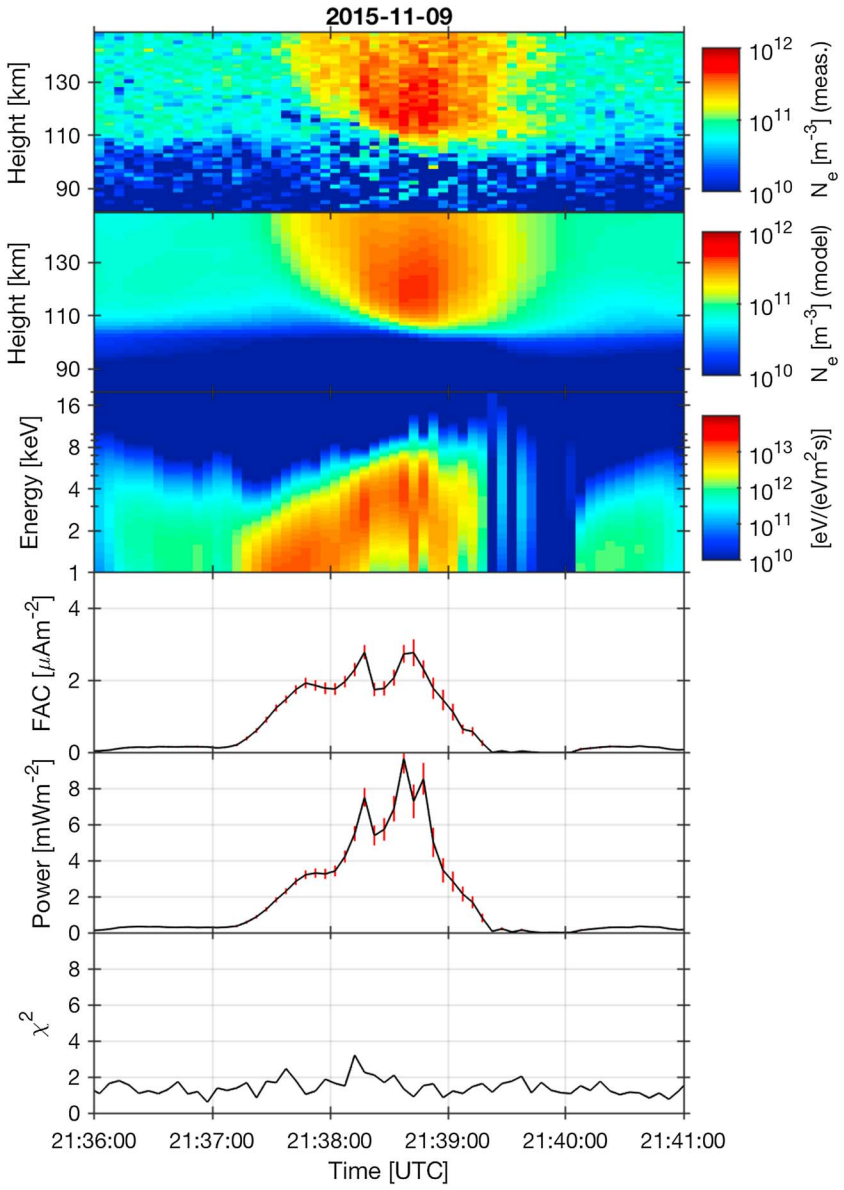

Figure 5. Inversion results during the Swarm C overflight on 9 November 2015. Electron density observed with EISCAT (top panel), electron density modeled in the inversion (second panel), differential energy flux (third panel), upward FAC (fourth panel), total energy flux (fifth panel), and χ^2 (bottom panel). The red vertical bars in the fourth and fifth panel are 1-σ error estimates. The satellite crossed the EISCAT geomagnetic latitude at 21:38:39 UT.

The modeled electron density profiles in the second panel of Figure 5 match well with the observed densities. The only difference is the local decrease between 115 and 130 km altitudes in the observed densities after 21:39:30, which is not reproduced in the inversion. The inverted energy spectra in the third panel show low fluxes of electrons below 4 keV until 21:37:15, when a larger flux is seen first at the low energies. The peak energy increases from 1 to 4 keV in about 80 s, until the peak energy and flux decrease rather sharply after 21:38:40, resulting in an inverted-V-like structure in peak energy (Frank & Ackerson, 1971). The flux estimates are very small from 21:39:20 to 21:40:05 UT, at the same time when the measured electron density values show a local depletion.

The observed local depletion in the electron density profiles is very similar to those observed in small-scale auroral structures by Lanchester et al. (1998), who explained the structure by plasma convection due to an electric field close to edge of the arc. Similar *bite-outs* were observed also by Dahlgren et al. (2011). The very small estimated electron fluxes may thus be underestimates, because the electrons and ions may have moved

out from the radar beam instead of recombining within the beam. Such plasma motion cannot be correctly interpreted by ELSPEC, because the convective derivative is not included in the electron continuity equation (1).

The fourth and fifth panels of Figure 5 show estimates of the upward FAC and the total energy flux, integrated from the differential number flux and the differential energy flux, correspondingly. The error bars are larger when the arc is within the beam because more parameters are needed to explain the more complex spectral shapes, the adaptive integration uses shorter time period of data for the inversion due to faster recombination, and data variances are larger due to incoherent scatter self-noise. The FAC varies from 1 to 3 μAm^{-2} and the total energy flux from 2 to 10 mWm^{-2} when strongest ionization is observed from 21:38 to 21:39 UT.

Estimates of FAC from Swarm C and the inversion results are compared in Figure 6. The FAC estimates from Swarm C vector magnetometer measurement with 1 s time resolution are calculated from single-satellite data assuming a sheet-like current, which are stored as Level 1b data in the Swarm data base (Ritter et al., 2013). The blue dash-dotted line in the upper panel is the Swarm C current density estimate as a function of geomagnetic latitude (aacgm_v2), multiplied with the ratio of magnetic field strengths at altitudes 100 and 438 km (altitude of Swarm C). The red dot with the vertical bar shows the inverted current density estimate at time of the overflight with the 1-σ error estimate. The inversion result corresponds to the 5 s radar integration 21:38:35 to 21:38:40 UT. The lower panel shows geomagnetic coordinates of the satellite (dotted lines) and the radar (continuous lines) as function of UT time. The points where the satellite crosses the Tromsø geomagnetic latitude are marked with vertical black dotted lines in the panels. At the time of the latitude crossing, the difference in geomagnetic longitudes of the satellite and the radar was about 0.7° and the shortest distance between the satellite and the radar beam was 36 km. The inverted estimate for the current density is 2.7$\pm$ 0.3 μAm^{-2}, while the Swarm C analysis gives 1.7 – 2.2 μAm^{-2}, so the estimates match rather nicely.

4.3. Electron Precipitation 9 November 2015

In the two sections above, the inversion was used for short events, where a possibility for satellite comparison was available. However, our aim is to use the radar inversion technique for longer duration observations of the electron energy spectra when continuous satellite data are not available. In order to demonstrate such observations, Figure 7 shows a 2-hr period of data from 9 November 2015. The auroral arc with simultaneous Swarm C overflight takes place around 21:39 UT. The data contain periods with various characteristics of the precipitation, from low fluxes of soft precipitation in the beginning to more intense fluxes with peak energies reaching several tens of keV in the latter half.

Both the FAC and the total energy flux are highly variable. The FAC is typically below 4 μAm^{-2} and the total energy flux below 25 mWm^{-2}. However, the FAC reaches 14 μAm^{-2} and the total energy flux 250 mWm^{-2} in association with intense precipitation around 22:15 UT. The estimated values are in accordance with earlier results: energy fluxes within auroral arcs are typically 5 – 30 mWm^{-2} (Dahlgren et al., 2011; Kaeppler et al., 2015; Stenbaek-Nielsen et al., 1998) and in dynamic aurora from tens (Kaeppler et al., 2015) to even several hundred mWm^{-2} (Lanchester et al., 1998). The FACs associated with auroral arcs also show a great variability just from a few to tens of μAm^{-2} and for very small scales even larger current densities (e.g., McGranaghan et al., 2017, and references therein).

Variations in the FAC are smaller than in the total energy flux in the studied event, because the contribution of the highly variable high-energy flux is larger in the total energy flux. One should also note that the upward FAC carried by electrons with energies below 1 keV is not included in the ELSPEC FAC estimates. Previous studies have shown that contribution of low-energy electrons to the FAC is small at ionospheric altitudes when the electrons are accelerated by quasi-static parallel potential drops (typically >1 keV; e.g., Olsson et al., 1998). However, low-energy electrons may provide an additional contribution to the current due to rapid time variability of the particle acceleration region (Morooka et al., 2004). The low-energy contribution to the FAC is more significant for Alfvenic aurora (Chaston et al., 2007).

The χ^2 estimates in the lowest panel of Figure 7 are very good (close to one) most of the time, but contain several sharp peaks 21:45 to 22:15 UT, when the observed electron density is highly variable in time. The vast majority of the peaks are associated with a rapid decrease of the electron density, which cannot be explained by the recombination model alone. We anticipate that the ions may have convected out of the radar beam, as explained by (Lanchester et al., 1998) and discussed already in section 4.2.

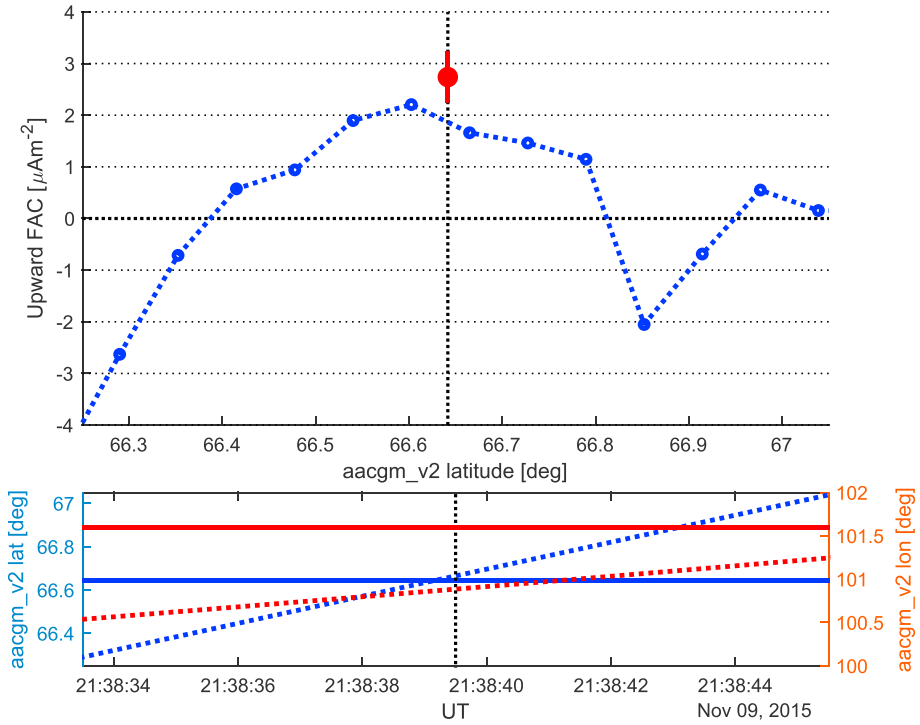

Figure 6. Comparison of field-aligned current estimated with ELSPEC and observations from the Swarm C satellite. Upper panel: FAC from Swarm C (blue) and inverted upward FAC from the time when the satellite crossed the EISCAT magnetic (aacgm_v2) latitude (red). The red vertical bar is the 1-σ error estimate from the inversion. The ELSPEC data point corresponds the 5 s radar integration 21:38:35 to 21:38:40 UT. Lower panel: aacgm_v2 coordinate of EISCAT (continuous lines) and Swarm C (dotted lines). The satellite crosses the EISCAT geomagnetic latitude 21:38:39 UT. The data points closest to the crossing are marked with black vertical dotted lines in the plots.

5. Discussion

Electron energy spectrum estimation from electron density profiles may be subject to various sources of uncertainty. Many of the sources are discussed by Semeter and Kamalabadi (2005), whose conclusions are valid also for the ELSPEC technique. We have tested the reliability of the technique both by means of analysis of simulated data and by means of comparisons to satellite data. In this section we discuss the effects of the poorly known ion composition, the effect of neglecting the plasma convection, some specific details of the ELSPEC technique, and the necessity of the time-dependent model.

5.1. Ion Composition and Recombination

The Electron recombination rate is a problematic issue in the energy spectrum inversion, because collisional ionization by precipitating electrons affects ion composition. Various approaches, including pure NO^+ composition (Semeter & Kamalabadi, 2005; Simon Wedlund et al., 2013) and simple functional forms for the recombination time scale (Brekke et al., 1989) have been used in previous studies. The composition issue is avoided if the ion chemistry is modeled as part of the inversion procedure (Turunen et al., 2016). We have reduced the problem by means of limiting the calculations to an altitude interval, where mainly O_2^+ and NO^+ ions are present. However, these two species have quite different recombination speeds, and errors in the O_2^+ to NO^+ ratio may still affect the results.

In order to quantify the error caused by the inaccurate composition, we have modeled the ion composition for the 9 November 2015 EISCAT UHF data with the SIC model, which solves concentrations of 16 neutral species and 72 ionic species (Turunen et al., 2009). The SIC model was preconditioned by means of modeling the 5 days before the event with photoionization alone. Ion production rates that lead to matching observed and modeled electron densities during the event were then determined for a number of altitudes. The model run produced densities of the neutral and ion species for each time step and height. Within the 80–150 km altitude interval, the ions were found to be almost solely O_2^+ and NO^+.

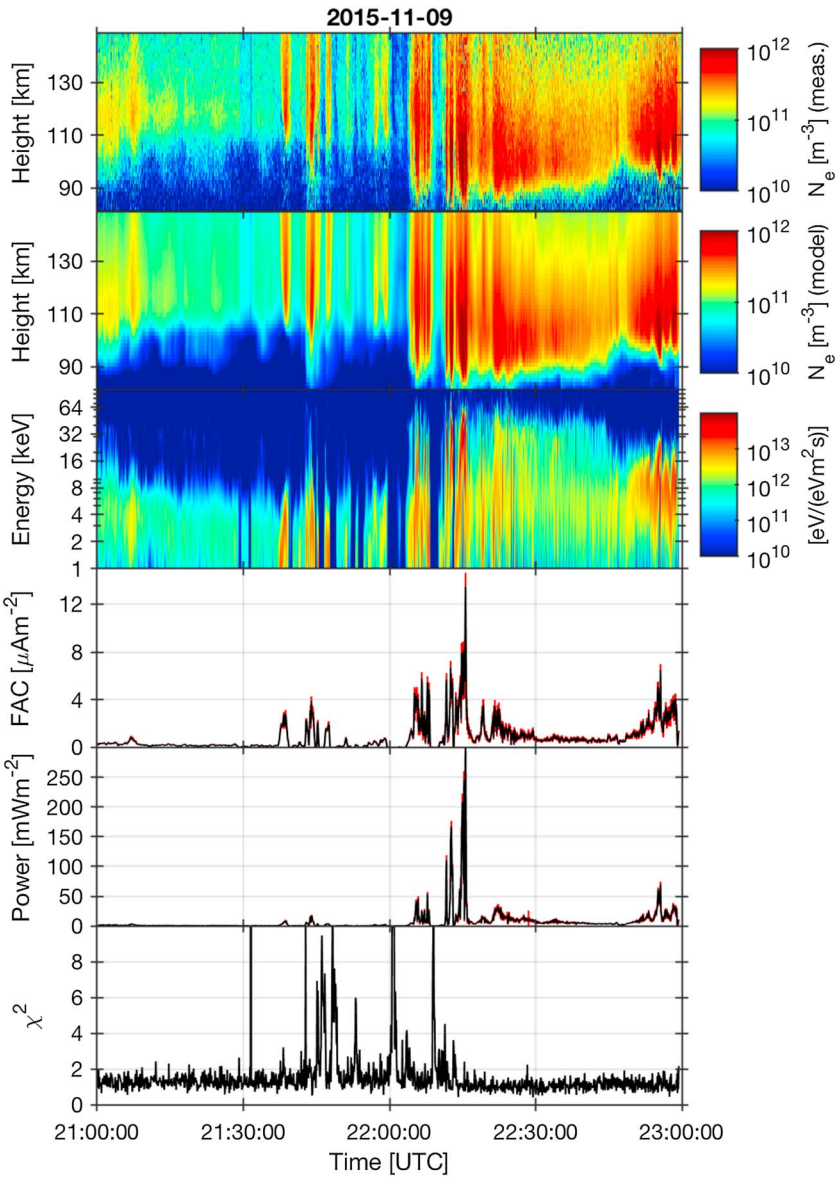

Figure 7. A 2-hr period of inversion results for 9 November 2015. Electron density observed with EISCAT (top panel), electron density modeled in the inversion (second panel), differential energy flux (third panel), upward FAC (fourth panel), total energy flux (fifth panel), and χ^2 (bottom panel). The red vertical bars in the fourth and fifth panel are 1-σ error estimates.

Figure 8 shows the measured electron density (first panel), the O_2^+/N_e fraction from the IRI model (second panel), the SIC-modeled O_2^+/N_e fraction (third panel), the differential energy flux estimated with the IRI compositions (fourth panel), and the difference of the spectrum estimates with the IRI and SIC compositions (fifth panel). The SIC model shows rapid variations in the O_2^+/N_e fraction. For example, the composition at 105 km altitude changes from 95% of NO^+ to almost 70% O_2^+ in 2 min between 22:03:30 and 22:05:30, when very energetic precipitation starts. In addition to the rapid variations, the SIC-modeled O_2^+/N_e fraction below 100 km is consistently much larger than the IRI output shown in the second panel of Figure 8. The difference of the two energy spectrum estimates in the bottom panel of Figure 8 indicates that the IRI composition leads to overestimation of the flux at the high-energy end of the spectrum and underestimation at the low-energy end, that is, the peak of the differential energy flux is at a higher energy with the IRI compositions than with the SIC compositions. A similar shift of the peak energy was reported by Semeter and Kamalabadi (2005) when ion composition was changed from pure NO^+ to pure O_2^+.

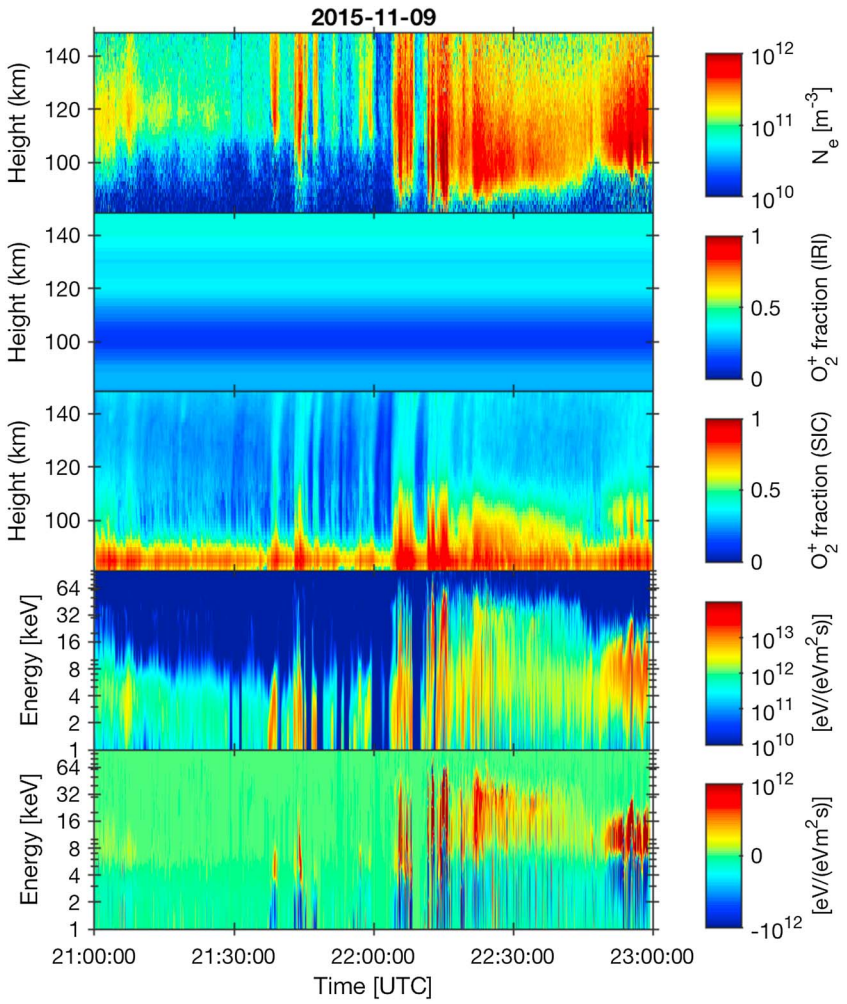

Figure 8. Effect of SIC-model ion compositions. Electron density (top panel), IRI O_2^+/N_e fraction (second panel), SIC O_2^+/N_e fraction (third panel), differential energy flux estimated with the IRI composition (fourth panel), and difference of differential energy fluxes calculated with IRI and SIC compositions (IRI-SIC; fifth panel). Notice that the last panel is in linear scale, while the spectra in the fourth panel are in logarithmic scale.

Figure 9 shows the measured electron density (top panel), the total energy flux estimates with IRI (red) and SIC (black) ion compositions (second panel), ratio of the two total energy flux estimates (third panel), upward FAC estimates with IRI (red) and SIC (black) compositions (fourth panel), and ratio of the two FAC estimates (fifth panel). The total energy flux ratio is shown only when the power is larger than 2 mWm^{-2} and the FAC ratio when the FAC is larger than 0.5 μAm^{-2}. The two compositions lead to very similar estimates of the total energy flux and FAC. From 21 to 22 UT both power and FAC estimates with the two composition models are almost identical. After 22 UT, when the lower boundary of ionization reaches the high O_2^+ concentration in the SIC model and more O_2^+ is produced also at upper altitudes, the power estimates calculated with IRI compositions are systematically larger than those calculated with the SIC compositions. The ratio of the two power estimates reaches 1.5 in a few individual points, but remains mostly below 1.2 also during the more intense precipitation. The difference in the FAC estimates is generally smaller than in the power estimates, which may be expected because the FAC estimates have larger contribution from low energies, that is, high altitudes, where the difference of the two ion composition models is smaller. Also, the ratio for the FACs gets values both above and below one, indicating that both overestimation and underestimation takes place.

Another composition issue is metallic ions, which recombine very slowly and are known to be abundant in sporadic E layers. This readily reveals that the inversion is not reliable in the presence of a sporadic E, but the effect of metallic ions when they are spread in altitude is less obvious. Based on rocket observations by Kopp (1997), the metallic ion density is typically less than 10^{10} m^{-3}. Exceptions to this are sporadic E lay-

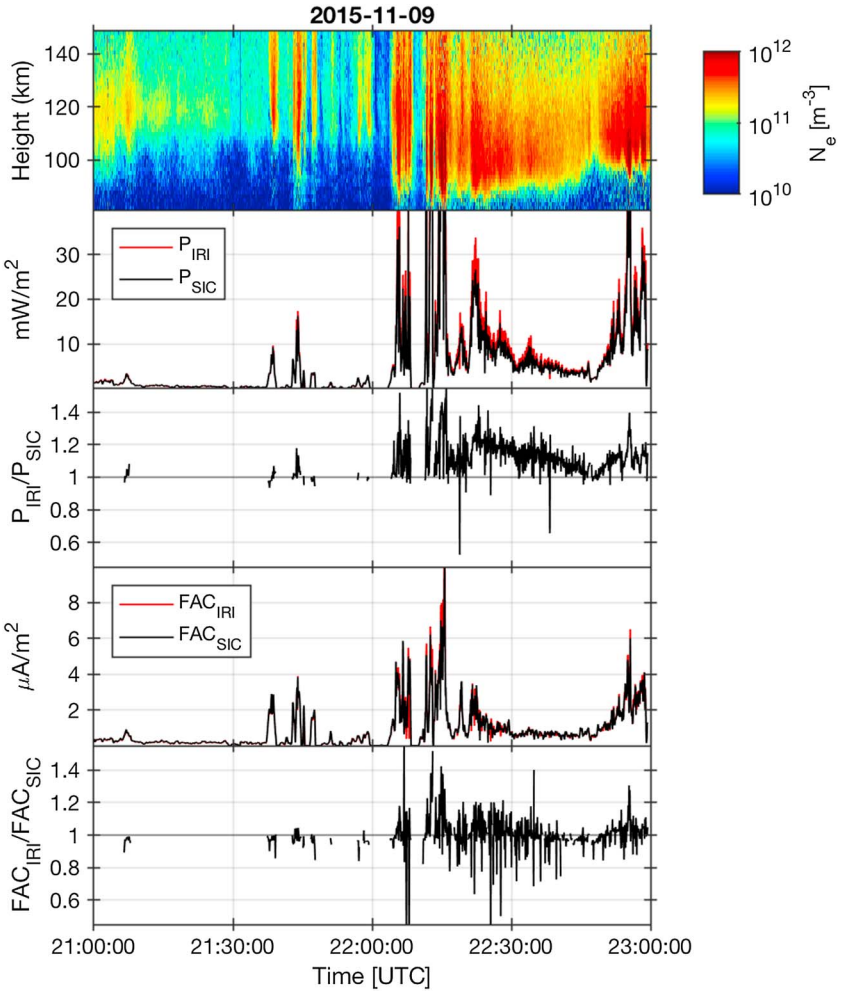

Figure 9. Effect of SIC-model ion compositions. Electron density (top panel), total precipitation power estimated with IRI (red) and SIC (black) compositions (second panel), ratio of the total precipitation power estimates (third panel), upward FAC estimated with IRI (red) and SIC (black) compositions (fourth panel), and ratio of the FAC estimates (fifth panel). The power ratio in the third panel is plotted only for points where the power is larger than 2 mWm^{-2} and the FAC ratio in the fifth panel only when the FAC is larger than 0.5 μAm^{-2}.

ers and intense meteor showers. Because electron precipitation does not affect the absolute concentration of metallic ions, we conclude that metallic ions might have an effect on the energy spectrum estimates when the electron densities are very small. However, electron densities associated with clearly nonzero FACs and energy fluxes are at least an order of magnitude above the metallic ion concentration, whose contribution is considered negligible in this case.

Errors caused by ion composition should be compared to the accuracy of the ion production model. Error estimates reported by Fang et al. (2010) for 1–100 keV electrons are 5% for the total electron production rate, 5% for the peak electron production rate, and less than 1 km for the peak ionization altitude. Errors in the production rates could thus cause about 5% error in the total energy flux estimates. Because the 1 km accuracy corresponds to about 1 keV difference in the peak energy when the peak is close to 10 keV, and Maxwellian fluxes with 10 keV and 11 keV peak energies and identical total number fluxes have 10% difference in the total energy flux, we conclude that inaccuracies in the ion production profiles may cause about 10% error in the total energy flux estimates. Other sources of uncertainty in the ion production rate include the neutral mass density profile from MSIS, which may be affected by auroral activity (Semeter & Kamalabadi, 2005), and errors in radar power calibration, which may be quite challenging in active, nighttime conditions. Based on the authors' experience, results from different calibration techniques may vary by 10%, which corresponds

to about 20% difference in the total number and energy fluxes. The error caused by the inaccurate ion composition is thus the largest well-quantified individual source of error, but its effect is still comparable to other sources of inaccuracy.

5.2. Effects of Electric Field

We have limited the analysis below 150 km altitude in order to avoid effects of plasma convection. However, this limit is not enough to guarantee that convection would never affect the results. Close to the edges of auroral arcs, convection may shift plasma produced within the radar beam out of it within a narrow height interval if the horizontal electric field is very large (Lanchester et al., 1998). Such a structure was observed also in our data, as discussed in section (4.2). However, this effect arises only in events with very large electric fields at the edges of auroral arcs. Inside auroral arcs, the electric fields are known to be rather small at ionospheric altitudes (e.g., Aikio et al., 2012).

Even in steady state conditions, in presence of a static electric field, the electric field may affect the electron density profile shape (Huuskonen et al., 1984), but this effect is significant only when electron density is very low, allowing ions to move before they recombine. In that case, the energy flux carried by precipitating electrons will also be extremely low, and the effect has no practical consequence for estimated fluxes.

5.3. Energy Limits and Spectrum Model

The energy grid used in ELSPEC covers typically the energies from 10 eV to 100 keV, but only energies above 1 keV are considered reliable. Electrons with energies less than 1 keV produce ionization mainly above 150 km altitude (Fang et al., 2010), which is the upper boundary for our calculations. Correspondingly, altitude of the peak ionization rate of 100 keV electrons is close to our lower boundary at 80 km altitude (Fang et al., 2010). Data from above 150 km altitude are not used due to the O^+ dominated ion chemistry and ion convection and data from below 80 km are not used due to the complex ion chemistry including positive and negative molecular ions, cluster ions, etc. Altitudes below 80 km and energies above 100 keV can be reached by means of modeling the full ion chemistry (Turunen et al., 2016), which leads to computationally heavy analysis and is beyond the scope of this work.

Instead of the spectrum models (equation (11), other parametric spectrum shapes could be implemented in ELSPEC. For example, classification into Maxwellian, kappa, mono-energetic, and broadband distributions (McIntosh & Anderson, 2014) might benefit from including explicit Maxwellian and kappa distribution models and their *accelerated* versions. However, energy spectrum of the electrons entering the ionosphere is affected also by secondary electrons and degraded primaries at energies below the acceleration potential drop (Evans, 1974; Kaeppler et al., 2014). Furthermore, the radar data may be spatially averaged over areas with different precipitation characteristics. A set of very general models, which allows a variety of even rather exotic spectrum shapes, is thus a strength.

Regarding the averaging in radar data, the diameter of the volume observed with the EISCAT UHF radar around 100 km altitude is about 1 km—an order of magnitude larger than the filament where the mono-energetic precipitation was found to be concentrated by Lanchester et al. (1997). Even narrower, fast evolving auroral filaments, associated with mono-energetic precipitation, were observed by Dahlgren et al. (2012). Recent observations by Dahlgren et al. (2015) suggest that at least two different accelerated electron populations may be present on the very same magnetic field-line. When this adds up with the effects of large electric fields within the fine-structure of auroral arcs (Lanchester et al., 1996), it is evident that the spatially and temporally averaged electron density data from the radar do not necessarily correspond to any of the characteristic spectrum shapes observed with satellites above or within the ionosphere.

5.4. When is the Time-Dependent Model Necessary?

So far, we have stated that the time-dependent inversion model is needed for realistic energy spectrum inversion when the electron density varies on time scales shorter than the electron recombination time, but we have not quantified what the effects of a steady state assumption actually are. The simulated data in section 3 offers us a simple means to demonstrate the effects of a steady state assumption ($\partial n/\partial t = 0$) in a time-dependent situation.

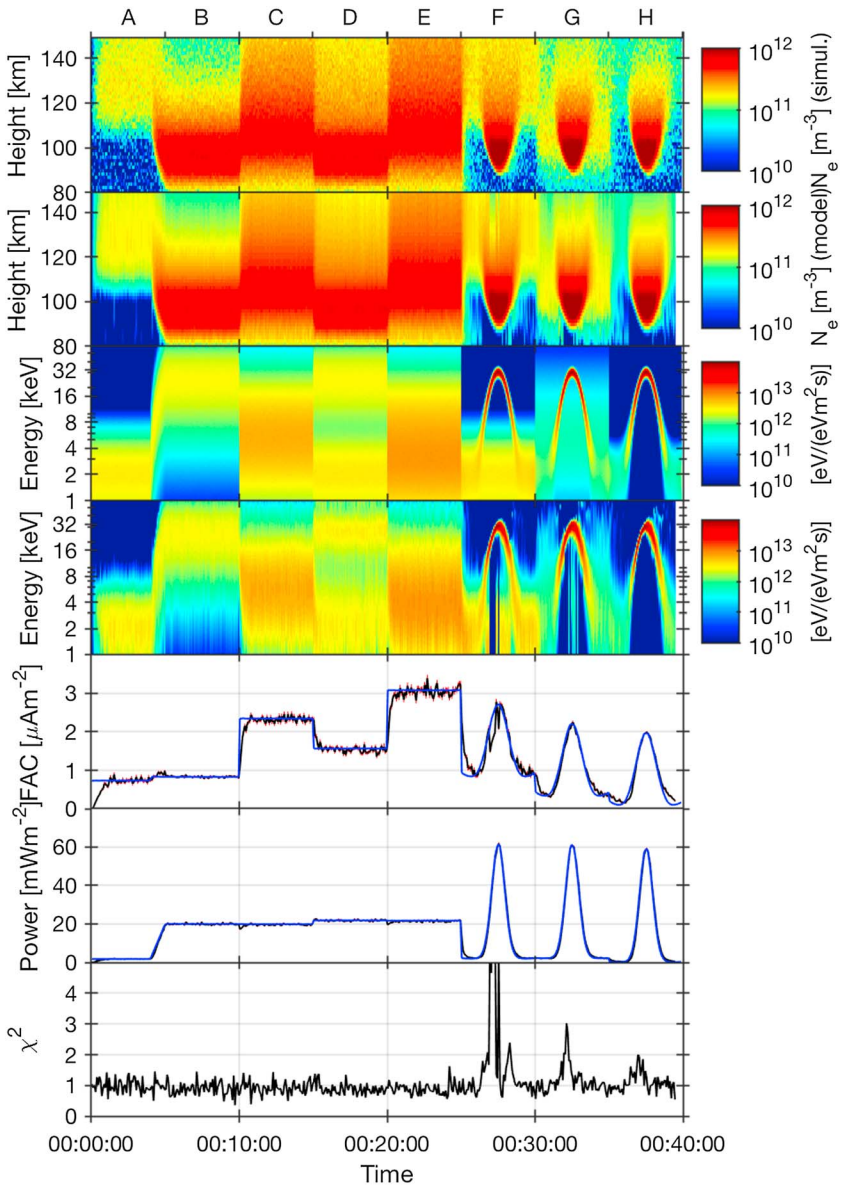

Figure 10. Simulated data analyzed with a steady state model. Simulated electron density (first panel), modeled electron density (second panel), differential energy flux used in the simulation (third panel), inverted differential energy flux (fourth panel), upward FAC (fifth panel), total energy flux (sixth panel) and χ^2 (bottom panel). The blue curves are the known simulation inputs and the black curves with red error bars are the inversion result.

The simulated data shown in Figure 1 is reanalyzed in otherwise identical manner with the time-dependent inversion, but the direct theory (equation (A2) is replaced with the steady state assumption

$$\mathbf{n}_k = \sqrt{\frac{\mathbf{Q}_k}{\boldsymbol{\alpha}_k}}. \tag{17}$$

The inversion result is shown in Figure 10. Comparing the calculated spectra in panel 4 from the top and the original spectra in panel 3 shows that the main characteristics of spectra are well reproduced, in much the same way as in the time-dependent calculation shown in Figure 1. However, the effect of the steady state model is seen especially at energies below 5 keV, where the flux rises too slowly at 00:10 and 00:20, and remains above the true level after 00:15 and 00:25. The whole low-energy part of the fourth panel of Figure 10

is shifted in time due to the steady state assumption. Interestingly, the mono-energetic distributions in periods F, G, and H show similar shifts also at energies above 20 keV. The results show clearly that estimation of accurate energy spectra at auroral energies requires time-dependent modeling.

Consequences of the steady state model are seen also in the FAC estimates, which tend to be below the true value when the electron density increases, and above the true value when the density decreases. In this simulation, for example, at 00:10 and 00:20, it takes about 40 s for the FAC estimate to reach the simulation value. This is a direct consequence of the bias at lower energies, which has a strong effect on the FAC estimates. However, when electron density increases gradually (periods G and H), FACs are rather well estimated.

For the total energy flux estimates, the effect is smaller. The energy flux estimates follow the known simulation input quite exactly, because the main contribution to the total energy flux is from the high-energy end of the spectra, which are less affected by the steady state model. In agreement with Lanchester et al. (1998) and Semeter and Kamalabadi (2005), we conclude that the total energy flux estimates are surprisingly tolerant against modeling error — even if the errors lead to clear bias in the differential energy flux.

6. Conclusions

We have developed a novel ELSPEC tool for estimating differential energy flux of precipitating electrons from incoherent scatter radar data. The technique is based on analytic integration of the electron continuity equation, fits with multiple parametric models of the spectrum shape, and model selection using the Akaike information criterion. This approach allows us to use data with almost arbitrary time resolutions, enables spectrum estimation with dense energy grids, avoids noise amplifications in numerical derivatives, and balances automatically between spectrum complexity and fitting to noise. ELSPEC can be used in both time-dependent and steady state modes and it calculates statistical error estimates for all its output parameters: differential number flux, differential energy flux, upward FAC, and total energy flux. Also, other parameters, for example, peak and average energies, can be extracted from the spectrum estimates. The spectrum models are general enough to produce, for example, Maxwellian, kappa, and mono-energetic spectra, as well as combinations of those.

The tool was verified by means of a simulation study and by means of comparisons to direct satellite observations in two case studies. The inversion results were found to agree well with the simulation inputs and the satellite data. A simulation study shows that proper time-dependent modeling of the electron density is crucial for realistic reconstruction of the electron energy spectra in time scales of seconds. The same applies to estimates of upward FAC, which are integrated from estimates of the differential electron number flux. The total energy flux is less sensitive to modeling errors, including the use of a steady state model.

With time resolutions coarser than the electron recombination time scale, the implicit assumption about constant precipitation during each time step makes the time-dependent model almost identical with the steady state model. With time resolutions of about a minute or longer, one can thus use the simpler steady state model. Estimation of the differential number or energy fluxes with coarse resolutions may not be reasonable in the rapidly varying high-latitude ionosphere. However, the total energy flux was found to be quite insensitive to errors in spectrum shape, and studies of the total energy flux may be most practical to conduct with time-averaged data and the steady state model.

Appendix A: Integrating the Electron Continuity Equation

The electron densities $\mathbf{n}(t)$ are solved by means of integrating the electron continuity equation (6). The solution can be written in the form

$$\mathbf{n}(t) = \frac{\mathbf{n}(t_{k-1}) + \sqrt{\mathbf{Q}_k/\boldsymbol{\alpha}_k}\tanh\left(\sqrt{\boldsymbol{\alpha}_k\mathbf{Q}_k}\,(t-t_{k-1})\right)}{\mathbf{n}\,(t_{k-1})\,\sqrt{\boldsymbol{\alpha}_k/\mathbf{Q}_k}\tanh\left(\sqrt{\boldsymbol{\alpha}_k\mathbf{Q}_k}(t-t_{k-1})\right)+1}\quad, t_{k-1}\le t\le t_k, \tag{A1}$$

where $\mathbf{Q}_k = \mathbf{A}_k\mathbf{I}_k$ is a vector of ion production rates for the time step k and $\boldsymbol{\alpha}_k$ is a vector of effective recombination coefficients.

A formula for the discrete electron density values $\mathbf{n}_k$ can be derived by means of substituting (equation (A1)) into (equation (7)). The solution is

$$\mathbf{n}_k = \frac{1}{\boldsymbol{\alpha}_k \Delta t}\left(\log\left(\frac{\mathbf{n}(t_{k-1})\sqrt{\boldsymbol{\alpha}_k/\mathbf{Q}_k}\tanh\left(\sqrt{\boldsymbol{\alpha}_k\mathbf{Q}_k}\Delta t\right)+1}{\tanh\left(\sqrt{\boldsymbol{\alpha}_k\mathbf{Q}_k}\Delta t\right)+1}\right)+\sqrt{\boldsymbol{\alpha}_k\mathbf{Q}_k}\Delta t\right). \tag{A2}$$

The special case $Q = 0$ in equations (A1) and (A2) never occurs in ELSPEC, because the models of differential number flux produce only positive values. One should notice that the electron density at previous time step in equation (A2) is not the averaged density $\mathbf{n}_{k-1}$, but the density at the end of the time step $\mathbf{n}(t_{k-1})$.

Appendix B: Adaptive Integration

The unrealistic oscillations in time can be suppressed by means of using a coarser time resolution. In order to implement this with a minimum impact on the spectrum estimates, the fit is performed for data from $m + 1$ successive time steps, but the later ones are included with smaller weights. The modified sum-of-squares to be minimized is

$$SS'_L = \sum \frac{\left[\left(\mathbf{N}_k;\mathbf{N}_{k+1};\ldots;\mathbf{N}_{k+m}\right)-\left(\mathbf{n}_k;\mathbf{n}_{k+1};\ldots;\mathbf{n}_{k+m}\right)\right]^2}{\left(\boldsymbol{\alpha}_k^2;\mathbf{S}_{k,1}\boldsymbol{\alpha}_{k+1}^2;\ldots;\mathbf{S}_{k,m}\boldsymbol{\alpha}_{k+m}^2\right)}, \tag{B1}$$

where the variance scales $\mathbf{S}$ depend on the electron recombination time scale $\theta_k = \left(\boldsymbol{\alpha}_k\mathbf{n}_k\right)^{-1}$,

$$\mathbf{S}_{k,m} = \exp\left(\frac{4m\Delta t}{\theta_k}\right). \tag{B2}$$

The number of time steps m is typical such that $m\Delta t \approx 30$ s. Because we are manipulating the variances, the Akaike information criterion is calculated as

$$AIC'_L = SS'_L + \frac{2(L+1)(L+2)}{M'-L}, \tag{B3}$$

where $M' = M + \sum_m \mathbf{S}_{k,m}^{-1}$.

The variance scales (equation (B2)) have been found to perform well, but the functional form is not based on theoretical considerations and might not be an optimal one. The highest possible time resolution Δt can be forced by means of selecting $m = 0$, and the time resolution reduces to Δt at the limit of a short recombination time scale.

Acknowledgments
Ilkka Virtanen is funded by the Academy of Finland, application number 285474. Ilkka Virtanen thanks the Vilho, Yrjö and Kalle Väisälä Foundation of the Finnish Academy of Science and Letters for financial support. EISCAT is an international association supported by research organizations in China (CRIRP), Finland (SA), Japan (NIPR and STEL), Norway (NFR), Sweden (VR), and the United Kingdom (NERC). The European Space Agency (ESA) is acknowledged for providing the Swarm data. The EISCAT data are available for download from the EISCAT web page (http://www.eiscat.se).

References

Aikio, A. T., Cai, L., & Nygrén, T. (2012). Statistical distribution of height-integrated energy exchange rates in the ionosphere. *Journal of Geophysical Research*, *117*, A10325. https://doi.org/10.1029/2012JA018078

Aikio, A. T., Lakkala, T., Kozlovsky, A., & Williams, P. J. S. (2002). Electric fields and currents of stable drifting auroral arcs in the evening sector. *Journal of Geophysical Research*, *107*(A12), 1424. https://doi.org/10.1029/2001JA009172

Asamura, K., Tsujita, D., Tanaka, H., Saito, Y., Mukai, T., & Hirahara, M. (2003). Auroral particle instrument onboard the INDEX satellite. *Advances in Space Research*, *32*(3), 375–378. https://doi.org/10.1016/S0273-1177(03)90275-4

Bilitza, D., Altadill, D., Zhang, Y., Mertens, C., Truhlik, V., Richards, P., et al. (2014). The international reference ionosphere 2012 – A model of international collaboration. *Journal of Space Weather and Space Climate*, *4*, 12. https://doi.org/10.1051/swsc/2014004

Brekke, A., Hall, C., & Hansen, T. L. (1989). Auroral ionospheric conductances during disturbed conditions. *Annals of Geophysics*, *7*(3), 269–280.

Burnham, K. P., & Anderson, D. R. (2002). *Model Selection and Multimodel Inference* (2nd ed.). New York: Springer.

Chaston, C. C. (2003). Properties of small-scale Alfvén waves and accelerated electrons from FAST. *Journal of Geophysical Research*, *108*(A4), 8003. https://doi.org/10.1029/2002ja009420

Chaston, C. C., Hull, A. J., Bonnell, J. W., Carlson, C. W., Ergun, R. E., Strangeway, R. J., & McFadden, J. P. (2007). Large parallel electric fields, currents, and density cavities in dispersive Alfvén waves above the aurora. *Journal of Geophysical Research*, *112*, A05215. https://doi.org/10.1029/2006ja012007

Dahlgren, H., Gustavsson, B., Lanchester, B. S., Ivchenko, N., Brändström, U., Whiter, D. K., et al. (2011). Energy and flux variations across thin auroral arcs. *Annals of Geophysics*, *29*, 1699–1712. https://doi.org/10.5194/angeo-29-1699-2011

Dahlgren, H., Ivchenko, N., & Lanchester, B. S. (2012). Monoenergetic high-energy electron precipitation in thin auroral filaments. *Geophysical Research Letters*, *39*, L20101. https://doi.org/10.1029/2012GL053466

Dahlgren, H., Lanchester, B. S., & Ivchenko, N. (2015). *Geophysical Research Letters*, *42*, 1290–1296. https://doi.org/10.1002/2015GL063173

Evans, D. S. (1974). Precipitating electron fluxes formed by a magnetic field aligned potential difference. *Journal of Geophysical Research*, *79*(19), 2853–2858. https://doi.org/10.1029/JA079i019p02853

Fang, X., Randall, C. E., Lummerzheim, D., Wang, W., Lu, G., Solomon, S. C., & Frahm, R. A. (2010). Parameterization of monoenergetic electron impact ionization. *Geophysical Research Letters*, *37*, L22106. https://doi.org/10.1029/2010GL045406

Frank, L. A., & Ackerson, K. L. (1971). Observations of charged particle precipitation into the auroral zone. *Journal of Geophysical Research*, *76*(16), 3612–3643. https://doi.org/10.1029/JA076i016p03612

Huuskonen, A., Nygrén, T., Jalonen, L., & Oksman, J. (1984). The effect of electric field-induced vertical convection on the precipitation E-layer. *Journal of Atmospheric and Terrestrial Physics*, *46*(10), 927–935. https://doi.org/10.1016/0021-9169(84)90033-3

Kaeppler, S. R., Hampton, D. L., Nicolls, M. J., Strømme, A., Solomon, S. C., Hecht, J. H., & Conde, M. G. (2015). An investigation comparing ground-based techniques that quantify auroral electron flux and conductance. *Journal of Geophysical Research: Space Physics*, *120*, 9038–9056. https://doi.org/10.1002/2015JA021396

Kaeppler, S. R., Nicolls, M. J., Strømme, A., Kletzing, C. A., & Bounds, S. R. (2014). Observations in the *E* region ionosphere of kappa distribution functions associated with precipitating auroral electrons and discrete aurorae. *Journal of Geophysical Research: Space Physics*, *119*, 10,164–10,183. https://doi.org/10.1002/2014JA020356

Karlsson, T. (2013). The acceleration region of stable auroral arcs. In A/ Keiling, E. Donovan, F. Bagenal, & T. Karlsson (Eds.), *Auroral phenomenology and magnetospheric processes: Earth and other planets* (pp. 227–239). Washington, DC: American Geophysical Union. https://doi.org/10.1029/2011GM001179

Keiling, A. (2009). Alfvén waves and their roles in the dynamics of the Earth's magnetotail: A review. *Space Science Reviews*, *142*, 73–156. https://doi.org/10.1007/s11214-008-9463-8

Kirkwood, S. (1988). SPECTRUM - a computer algorithm to derive the flux-energy spectrum of precipitating particles from EISCAT electron density profiles (*Tech. Rep. 34*). Kiruna, Sweden: Swedish Institute of Space Physics.

Kletzing, C. A., Scudder, J. D., Dors, E. E., & Curto, C. (2003). Auroral source region: Plasma properties of the high-latitude plasma sheet. *Journal of Geophysical Research*, *108*(A10), 1360. https://doi.org/10.1029/2002JA009678

Kopp, E. (1997). On the abundance of metal ions in the lower ionosphere. *Journal of Geophysical Research*, *102*(A5), 9667–9674. https://doi.org/10.1029/97JA00384

Lanchester, B. S., Kaila, K., & McCrea, I. W. (1996). Relationship between large horizontal electric fields and aruroral arc elements. *Journal of Geophysical Research*, *101*(A3), 5075–5084. https://doi.org/10.1029/95JA02055

Lanchester, B. S., Palmer, J. R., Rees, M. H., Lummerzheim, D., Kaila, K., & Turunen, T. (1994). Energy flux and characteristic energy of an elemental auroral structure. *Geophysical Research Letters*, *21*(25), 2789–2792. https://doi.org/10.1029/94GL01764

Lanchester, B. S., Rees, M. H., Lummerzheim, D., Otto, A., Frey, H. U., & Kaila, K. U. (1997). Large fluxes of auroral electrons in filaments of 100 m width. *Journal of Geophysical Research*, *102*(A5), 9741–9748. https://doi.org/10.1029/97JA00231

Lanchester, B. S., Rees, M. H., Sedgemore, K. J. F., Palmer, J. R., Frey, H. U., & Kaila, K. U. (1998). Ionospheric response to variable electric fields in small-scale auroral structrures. *Annals of Geophysics*, *16*, 1343–1354. https://doi.org/10.1007/s00585-998-1343-8

Lehtinen, M. S., & Huuskonen, A. (1996). General incoherent scatter analysis and GUISDAP. *Journal of Atmospheric and Terrestrial Physics*, *58*, 435–452. https://doi.org/10.1016/0021-9169(95)00047-X

McFadden, J. P., Carlson, C. W., & Ergun, R. E. (1999). Microstructure of the auroral acceleration region as observed by FAST. *Journal of Geophysical Research*, *104*(A7), 14,453–14,480. https://doi.org/10.1029/1998JA900167

McGranaghan, R. M., Mannucci, A. J., & Forsyth, C. (2017). A comprehensive analysis of multiscale field-aligned currents: Characteristics, controlling parameters, and relationships. *Journal of Geophysical Research: Space Physics*, *122*, 11,931–11,960. https://doi.org/10.1002/2017JA024742

McIntosh, R. C., & Anderson, P. C. (2014). Maps of precipitating electron spectra characterized by Maxwellian and kappa distributions. *Journal of Geophysical Research: Space Physics*, *119*, 10,116–20,232. https://doi.org/10.1002/2014JA020080

Miyoshi, Y., Oyama, S., Saito, S., Kurita, S., Fujiwara, H., & Kataoka, R. (2015). Energetic electron precipitation associated with pulsating aurora: EISCAT and Van Allen Probe observations. *Journal of Geophysical Research: Space Physics*, *120*, 2754–2766. https://doi.org/10.1002/2014JA020690

Morooka, M., Mukai, T., & Fukunishi, H. (2004). Current-voltage relationship in the auroral particle acceleration region. *Annales Geophysicae*, *22*, 3641–3655. https://doi.org/10.5194/angeo-22-3641-2004

Mozer, F., Cattell, C. A., Hudson, M. K., Lysak, R. L., Temerin, M., & Torbert, R. B. (1980). Satellite measurements of low altitude auroral particle acceleration. *Space Science Reviews*, *27*, 155–213. https://doi.org/10.1007/BF00212238

Newell, P. T., Sotirelis., T., & Wing, S. (2009). Diffuse, monoenergetic, and broadband aurora: The global precipitation budget. *Journal of Geophysical Research*, *114*, A09207. https:/doi.org/10.1029/2009JA014326

Olsen, N., Friis-Christensen, E., Floberghagen, R., Alken, P., Beggan, C. D., Chulliat, A., et al. (2013). The Swarm satellite constellation application and research facility (scarf) and Swarm data products. *Earth, Planets and Space*, *65*, 1189–1200. https://doi.org/10.5047/eps.2013.07.001

Olsson, A., Andersson, L., Eriksson, A. I., Clemmons, J., Erlandsson, R. E., Reeves, G., et al. (1998). Freja studies of the current-voltage relation in substorm-related events. *Journal of Geophysical Research*, *103*(A3), 4285–4301. https://doi.org/10.1029/97JA00560

Palmroth, M., Janhunen, P., Germany, G., Lummerzheim, D., Liou, K., Baker, D. N., et al. (2006). Precipitation and total power consumption in the ionosphere: Global MHD simulation results compared with Polar and SNOE observations. *Annales Geophysicae*, *24*, 861–872. https://doi.org/10.5194/angeo-24-861-2006

Pavlov, A. V. (2012). Ion chemistry of the ionosphere at E- and F-region altitudes: A review. *Surveys in Geophysics*, *33*, 1133–1172. https://doi.org/10.1007/s10712-012-9189-8

Picone, J. M., Hedin, A. E., Prob, D. B., & Aikin, A. C. (2002). NRLMSISE-00 empirical mode of the atmosphere: Statistical comparison and scientific issues. *Journal of Geophysical Research*, *107*(A12), 1468. https://doi.org/10.1029/2002JA009430

Rietveld, M. T., Wright, J. W., Zabotin, N., & Pitteway, M. L. V. (2008). The Tromsø dynasonde. *Polar Science*, *2*, 55–71. https://doi.org/10.1016/j.polar.2008.02.001

Ritter, P., Lühr, H., & Rauberg, J. (2013). Determining field-aligned currents with the Swarm constellation mission. *Earth, Planets and Space*, *65*, 1285–1294. https://doi.org/10.5047/eps.2013.09.006

Saito, H., Mizuno, T., Tanaka, K., Sone, Y., Fukuda, S., Sakai, S.-I., et al. (2005). An overview and initial in-orbit status of "INDEX" satellite. In *proceedings of the 20th Annual AIAA/USU Conference on Small Satellites*, Japan, pp. SSC06–IV–1.

Semeter, J., & Kamalabadi, F. (2005). Determination of primary electron spectra from incoherent scatter radar measurements of the auroral *E* region. *Radio Science*, *40*, RS2006. https://doi.org/10.1029/2004RS003042

Sheehan, C. H., & St-Maurice, J.-P. (2004). Dissociative recombination of N_2^+, O_2^+, and NO^+: Rate coefficients for ground state and vibrationally excited ions. *Journal of Geophysical Research*, *109*, A03302. https://doi.org/10.1029/2003JA010132

Shepherd, S. G. (2014). Altitude-adjusted corrected geomagnetic coordinates: Definition and functional approximations. *Journal of Geophysical Research: Space Physics*, *119*, 7501–7521. https://doi.org/10.1002/2014JA020264

Simon Wedlund, C., Lamy, H., Gustavsson, B., Sergienko, T., & Brändström, U. (2013). Estimating energy spectra of electron precipitation above auroral arcs from ground-based observations with radar and optics. *Journal of Geophysical Research: Space Physics*, *118*, 3672–3691. https://doi.org/10.1002/jgra.50347

Solomon, S. C., Hays, P. B., & Abreu, V. J. (1988). The auroral 6300 Å emission: Observations and modeling. *Journal of Geophysical Research*, *93*(A9), 9867–9882. https://doi.org/10.1029/JA093iA09p09867

Stenbaek-Nielsen, H. C., Hallinan, T. J., Osborne, D. L., Kimball, J., Chaston, C., McFadden, J., et al. (1998). Aircraft observations conjugate to fast: Auroral are thicknesses. *Geophysical Research Letters*, *25*(12), 2073–2076. https://doi.org/10.1029/98GL01058

Turunen, E., Kero, A., Verronen, P. T., Miyoshi, Y., Oyama, S.-I., & Saito, S. (2016). Mesospheric ozone destruction by high-energy electron precipitation assciated with pulsating aurora. *Journal of Geophysical Research-Atmospheres*, *121*, 11,852–11,861. https://doi.org/10.1002/2016JD025015

Turunen, E., Verronen, P. T., Seppälä, A., Rodger, C. J., Clilverd, M. A., Tamminen, J., et al. (2009). Impact of different energies of precipitating particles on NO_x generation in the middle and upper atmosphere during geomagnetic storms. *Journal of Atmospheric and Solar - Terrestrial Physics*, *71*, 1176–1189. https://doi.org/10.1016/j.jastp.2008.07.005

Vierinen, J., Bhatt, A., Hirsch, M. A., Strømme, A., Semeter, J. L., Zhang, S.-R., & Erickson, P. J. (2016). High temporal resolution observations of auroral electron density using superthermal electron enhancement of Langmuir waves. *Geophysical Research Letters*, *43*, 5979–5987. https://doi.org/10.1002/2016GL069283

Vondrak, R. R., & Baron, M. J. (1977). *A method of obtaining the energy distribution of auroral electrons from incoherent scatter radar measurements, in Radar probing of the auroral plasma Edited by* A. Brekke, pp. 315–330. Tromsoe, Norway: Universitetsforlaget.